2-D Axisymmetric Simulation of the Electrochemical Machining of Internal Precision Geometries

M. Hackert-Oschätzchen[*, 1], M. Kowalick[1], R. Paul[1], M. Zinecker[1], D. Kuhn[1], G. Meichsner[2], A. Schubert[1,2]

[1] Professorship Micromanufacturing Technology, Technische Universität Chemnitz, 09107 Chemnitz, Germany

[2] Fraunhofer Institute for Machine Tools and Forming Technology, 09126 Chemnitz, Germany

* matthias.hackert@mb.tu-chemnitz.de

Abstract: In several fields of mechanical engineering internal precision geometries are applied. For example for shaft-hub connections various shapes of internal geometries are needed, like involute splines or feather key grooves. For this application requirements like high shape accuracy, sufficient stability, high wear resistance or an increase of life time have to be fulfilled. However, there is also a demand on quick and precise manufacturing processes that are flexibly in machining various internal geometries. Electrochemical machining (ECM) is a process which meets these requirements. This process allows surface structuring and shaping of metal components with high shape accuracy independently of the materials strength and hardness [1].

This study presents investigations on a developed process design for manufacturing internal precision geometries by pulsed electrochemical machining (PECM) with help of multiphysics simulations. Therefore a 2-D axisymmetric transient model was created. The considered physical phenomena are fluid dynamics, thermodynamics, electrodynamics, the formation and transport of hydrogen as well as geometry deformation. The resulting geometry is calculated for a machining time up to 250 s applying the developed model. The model allows a detailed prediction of the material removal process and helps to perform further developments and optimisations in the process design.

Keywords: Electrochemical Machining, anodic dissolution, precise internal geometries

1 Introduction

Internal precision geometries are applied for example for shaft-hub connections. Here shapes like involute splines or feather key grooves are needed. In these cases a precise manufacturing of these structures within a small tolerance range have to be realized. Furthermore, there can be a high material stress on the parts in use. For this wear resistant materials are needed. These materials are characterized amongst other things by a high hardness and thus they can be processed difficultly by cutting technologies. In the case of internal precision geometries broaching can be used for manufacturing. Here the broaching tool is sophisticated to manufacture and therefore expensive. Furthermore the geometries which can be machined are limited. So there is a demand on quick and precise manufacturing processes that are flexibly in machining various internal geometries and independently of the materials strength and hardness of the workpieces. Electrochemical machining (ECM) is a process which meets these requirements.

For the manufacturing of internal precision geometries pulsed electrochemical machining (PECM) was chosen. This process is a further development of EC-lowering and is characterized by a moving cathode and pulsed direct current [2, 3]. Figure 1 schematically shows the principle of a pulsed electrochemical machining process.
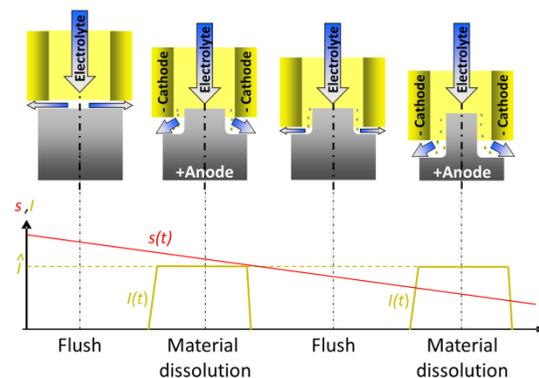
Figure 1. Scheme of the principle of a pulsed electrochemical machining process [4]

The workpiece, marked gray, is connected to the positive electrical pole of a power supply. The yellow marked cathode is connected to the negative pole and is moved with a defined feed rate towards the workpiece. During the process a suf-

ficiently conductive electrolyte is flushed through the working gap between workpiece and cathode. The material dissolution occurs during the electric current pulse in the pulse-on time. After that the electric current is paused, which is referred as pulse-off time. Within this time reaction products like hydrogen, dissolved material as well as process heat are transported out of the machining area, before a new electric current pulse is triggered. This strategy leads to enhanced accuracy of the production process.

In contemporary praxis, the design of the manufacturing process is a time-consuming and cost-intensive empirical procedure. Especially, the process design of machining internal geometries is difficult, because the shaping of the workpiece is effected perpendicular to the feed direction. Therefore, the peripheral working distance has to be determined, which is dependent on various process parameters. This study presents investigations on a developed process design by the help of multiphysics simulations.

2 Model Description

2.1 Geometry and Materials

For machining internal precision geometries by PECM a design concept was developed. Figure 2 shows in a 3-D CAD model the basic structure of the concept.
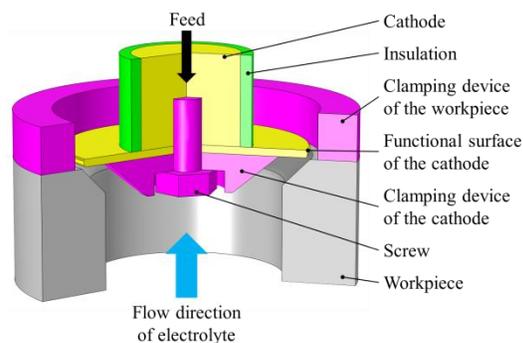

Figure 2. Design concept for machining internal precision geometries with pulsed electrochemical machining

As it can be seen, the concept has a nearly axisymmetric geometry. The main components are the workpiece, a lateral insulated cathode on which a replaceable disk with the functional surface of the cathode is mounted, as well as various clamping elements. The workpiece has an outer diameter of 44 mm and the pre-drilled bore has a diameter of 25 mm. The edge of the bore features a chamfer. The aspired diameter of the bore which is to be machined by PECM is 32 mm. For this, a cylindrical cathode disk with 31.6 mm in diameter

was investigated. The cathode moves with constant feed rate v_f of 1 mm/min towards the workpiece and machines the bore. The electrical pulsation during the machining process is considered in a time-averaged material dissolution velocity. The electrolyte flows from the bore into a flushing chamber, which is represented by the clamping element of the workpiece. With this flushing concept the working gap is permanently flushed with new electrolyte. To ensure the high precision machining it is necessary to carry the formed heat and reaction products away. These reaction products are for example hydrogen and dissolved material. The chosen flushing strategy should meet these requirements.

Based on the design concept of the machining process a 2-D axisymmetric model was derived. Figure 3 shows the geometry of the model containing the numbering of domains and boundaries.
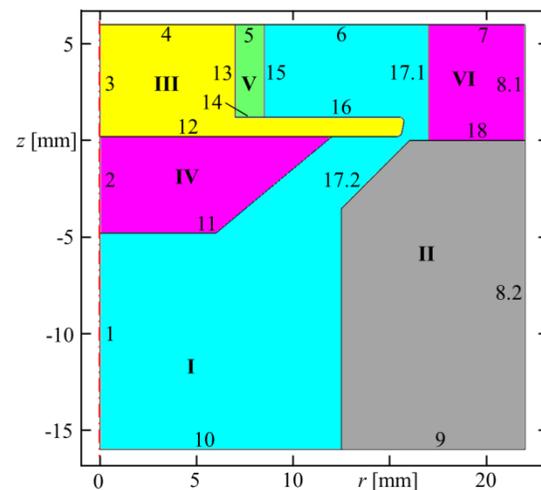
Figure 3. 2-D axisymmetric geometry of the model containing the numbering of domains and boundaries at initial time $t = 0$ s

Domain I is defined as fluid and represents the aqueous electrolyte with a mass fraction of 8% sodium nitrate ($NaNO_3$). The grey domain II is the solid workpiece. It is defined with the material properties of SAM 10, a powder-metallurgical material. For the yellow marked cathode (domain III) as well as for the workpiece clamping element (domain VI) stainless steel 1.4301 was chosen. The insulation (domain V) and clamping element (domain IV) are made from POM. Further information of the defined parameters is listed in table 1.

The effective electrical conductivity σ_{eff} of the electrolyte interspersed with hydrogen bubbles is defined by equution (1). Here the experimentally determined conductivity of the pure electrolyte with a mass fraction of 8% $NaNO_3$ is considered as a function of temperature T. In addition the

produced gas volume has influence on the electrical conductivity of the fluid in the working gap. This is taken into account by the electrolyte volume concentration ϕ_{El} by the term $\phi_{El}^{3/2}$[5, 6].

$$\sigma_{eff}(\phi_{El}, T) := \left(1.646 \, \frac{mS}{cm} \left(\frac{T}{1K} - 273.15 \right) + 39.796 \, \frac{mS}{cm} \right) \cdot \phi_{El}^{\frac{3}{2}}$$

(1)

Table 1: Allocation of material parameters

Domain	Material	σ [S/m]	λ [W/(m·K)]	c_P [J/(kg·K)]
I	Electrolyte	$\sigma_{eff}(\phi_{El},T)$	0.599	3877
II, VI	SAM 10	$1.69 \cdot 10^6$	21.5	410
III	1.4301	$1.37 \cdot 10^6$ [7]	15 [7]	500 [7]
IV, V	POM	10^{-10}	0.31 [8]	1500 [8]

2.2 Meshing

For the FEM simulation of the machining process of internal precision geometries an unstructured mesh was used. The mesh for the calculation shows figure 4.
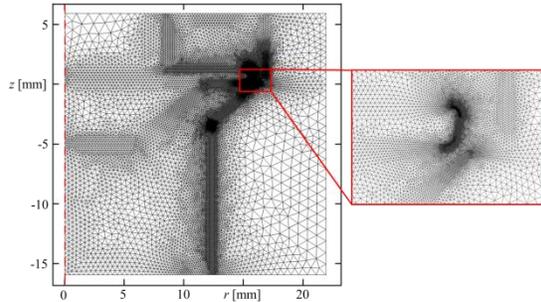
Figure 4. FEM mesh for the calculation of material dissolution

To generate this unstructured mesh a user-defined mesh was chosen. In the mesh settings the minimum element size is defined as 1 µm and the maximum element size as 1000 µm. The resolution of narrow regions, as it is inside the working gap, is set to 30 elements with a size of 4 µm in maximum. These settings lead to an initial mesh with 31683 elements. During the simulation the geometry is deformed to describe both the cathode feed and the material removal. In consequence of this a distortion of the mesh occurs. With the automatic remeshing option of COMSOL it is possible to define criteria when remeshing starts. For this the distortion was set to a maximum of 0.5. This leads to 130000 mesh elements at the end of the simulation.

2.3 Physics

The investigation of machining internal precise geometries was performed with a fully coupled model. In this connection the interfaces of heat transfer in fluids, electric currents and deformed geometry were used. The formation and transport of hydrogen gas was modeled with a partial equation in the area of the electrolyte.

The fluid dynamics was solved only in domain I of the simulation model. It is modeled by a potential two phase flow. The potential flow equation simplifies the modeling of the fluid flow and is characterized by inviscidness and irrotationality. In this connection the velocity field is determined as the gradient of the velocity potential ϕ. Due to the simplification the turbulent mass and heat transfer cannot be considered in detail. To enable a simplified description of these turbulent transport processes artificial diffusion terms were introduced using the artificial diffusion coefficient $v_K = 10^{-6}$ m²/s.

The flow inlet was set to boundary 10. Equation 2 describes the inflow of the electrolyte.

$$\nabla\phi \cdot \vec{n} = \frac{\dot{V}_{El}}{A_{In}}$$

(2)

Here $\vec{n}$ is the boundary normal vector. The flow rate $\dot{V}_{El}$ is set to 8 l/min and A_{In} corresponds to the cross-sectional area of the bore. The outlet is defined on boundary 6 with $\phi = 0$ m²/s.

The fluid pressure is modeled using Bernoulli's equation. Due to the inviscidness of the flow the pressure loss along the working gap cannot be inherently described by the potential equation. Therefore, a simplified description of the pressure loss was developed. In this connection the total pressure at an arbitrary point is interpolated between the inlet pressure 10.3 bar and the outlet pressure 5.5 bar as a linear function of the length of the streamline which the point is located on. The streamline length in the working gap was calculated using an additional partial differential equation.

The production of hydrogen along the cathode (boundary 16) is described with equation 3.

$$\Phi_{H_2,n} = - \frac{M_{H_2}}{2\,F} \hat{J}_n$$

(3)

As it can be seen the normal hydrogen mass flow density $\Phi_{H_2,n}$ depends on the normal electric current density $\hat{J}_n$. M_{H_2} is the molar mass of hydrogen and F is the Faraday constant.

The interface of thermodynamics is solved for all domains. Joule heating is considered in the fluid and solid domains. Furthermore, Joule heating is also regarded on the electrode-electrolyte interfaces according to the overpotentials which occur in the electrochemical double layer. On boundaries 4, 8 and 10 the ambient temperature of 20 °C is defined.

Regarding electrodynamics the boundary condition electric insulation is used on boundaries 5 to 7, 9 and 10. The ground potential is set to boundary 4. The process voltage U is set to 14 V. According to experimental results the cathodic and anodic overpotential are set to $U_{OC} = 1$ V and $U_{OA} = 5$ V. These overpotentials are defined homogeneously distributed on the electrode-electrolyte interfaces. On boundaries 8.1 and 8.2 the electric potential $\hat{\varphi}$ it is set according to equation 5.

$$\hat{\varphi} = U - U_{OC} - U_{OA}$$

(5)

A summary of the boundary conditions of the electric current interface according to figure 3 are listed in table 1.

Table 1. Boundary conditions in the interface electric currents for the boundaries numbered in figure 3

Boundary	Definition
1-3	Axis of symmetry
5-7, 9, 10	$\hat{J}_n = 0 \text{ A/cm}^2$
4	$\hat{\varphi} = 0 \text{ V}$
8.1, 8.2	$\hat{\varphi} = U - U_0; \ U_0 = 6 \text{ V}$

Based on the calculated electric current density on the workpiece surface the simulation of the material dissolution was carried out using the deformed geometry interface. In current investigations the effective material removal rate V_{eff} can be determined by the material-specific removal velocity in z-direction v_a and the corresponding current density J using equation 6 [9].

$$V_{eff} = \frac{v_a(J)}{J}$$

(6)

For this removal experiments have to be performed with the workpiece material and the machine, which are used for the aspired manufacturing process. For PECM the material dissolution occurs during the pulse-on time of the pulsed current. This pulsed current is characterized by the duty cycle c_I which is identified by the frequency f_p and by the pulse-on time t_{on} [9].

$$c_I = f_p \cdot t_{on}$$

(7)

Due to the pulsed electric current in PECM the velocity of the material removal is reduced compared with ordinary ECM. The time-averaged material removal velocity $\vec{v}_{a,c_I}$ corresponds to equation 8 [9].

$$\vec{v}_{a,c_I} = \vec{v}_a(\hat{J}_n) \cdot c_I$$

(8)

Here $\hat{J}_n$ is the normal electric current density during pulse-on time. In the removal experiments of SAM 10 a duty cycle of $c_I = 0.8$ was used. The results of these experimental investigations are shown in figure 5.
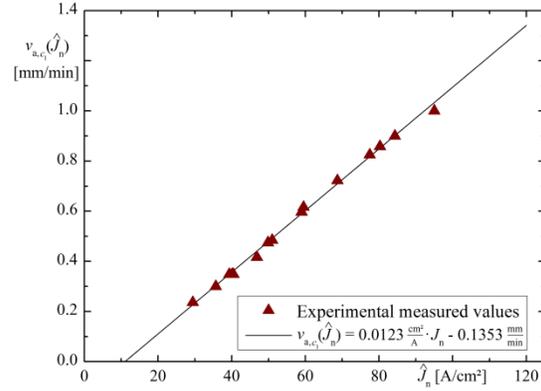
Figure 5. Material-specific removal velocity in z-direction v_a and the corresponding current density J for SAM 10

As it can be seen the experimental measured values lead to an empirical removal velocity function for SAM 10. It was found, that SAM 10 shows a transpassive dissolution behavior with the used $NaNO_3$ electrolyte. This behavior is implemented using equation 9. Boundary 17.2, which is to be machined, is assigned to this condition.

$$v_{a,c_I}(\hat{J}_n) = \begin{cases} 0 \ \dfrac{\text{mm}}{\text{min}} & \text{for } \hat{J}_n < 11 \ \dfrac{\text{A}}{\text{cm}^2} \\ (0{,}0123 \ \dfrac{\text{cm}^2}{\text{A}} \cdot \hat{J}_n - 0{,}1353 \ \dfrac{\text{mm}}{\text{min}} \\ \qquad \text{for } \hat{J}_n \geq 11 \ \dfrac{\text{A}}{\text{cm}^2} \end{cases}$$

(9)

Table 2 summaries the machining parameters used in this study.

Table 2. Summary of parameters used in modelling the machining of internal precision geometries

| Symbol	Name	Value
v_F	Feed velocity	1 mm/min
U	Voltage	14 V
c_I	Duty cycle	0,8
$\dot{V}_{El}$	Electrolyte flow	8 l/min
p_{Out}	Outlet absolute pressure	5,5 bar
T_U	Ambient Temperature	20 °C

3. Results of the Simulation

In figure 6 the result of the time-dependent calculation of the fluid flow after a processing time of 250 s is shown by means of a streamline false color rendering. The false color represents the flow velocity.
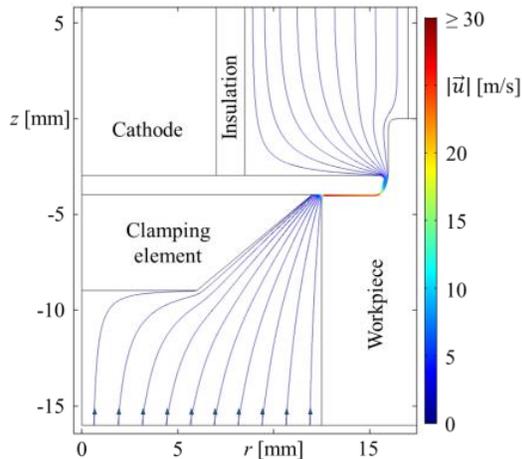
Figure 6. Streamline false color rendering of the fluid flow at $t = 250$ s

It can be seen, that the electrolyte enters the simulation area through the bore of the workpiece. Afterwards it flows through the working gap, where an acceleration of the flow velocity can be observed as a consequence of a decreasing cross-sectional area. Subsequently, at the exit of the working gap the cross-sectional area increases and hence the flow velocity drops. After that the fluid exits the simulation area through the upper boundary of the model that represents the flushing chamber.
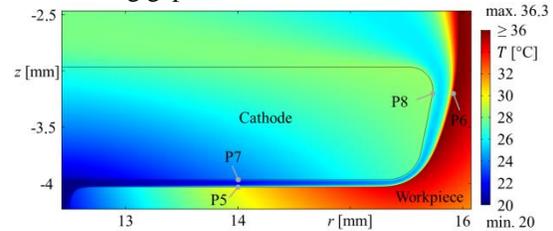
A detailed view of the velocity field within the working gap is shown in figure 7.
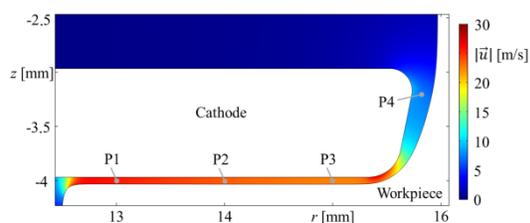
Figure 7. Detailed view of the velocity field within the working gap at $t = 250$ s

It can be seen, that the maximum of flow velocity is located in the working gap entering area. At point P1 there can be observed a velocity of 25.6 m/s. Along the gap the velocity decreases to 23.7 m/s at P2, 22.5 m/s at P3 and 7.5 m/s within the lateral gap at P4. Due to the high flow velocity within the working gap there is a good exchange of electrolyte and therefore also a transportation of reaction products.

In the machining process Joule heating occurs and the temperature along the working gap rises. The result of the simulation of the heat transfer interface is shown in figure 8 in a detailed view of the working gap at $t = 250$ s.

Figure 8. Detailed view of the temperature field within the working gap at $t = 250$ s

Here the electrolyte is entering the working gap with a temperature of 20 °C and is heated to about 26 °C to 27 °C in average along the gap. At the surface of the cathode temperatures of 23.9 °C in point 7 and 28.3 °C in point 8 can be observed. The temperatures at the workpiece surface are higher than at the cathode surface. In P5 there is 30.1 °C and in P6 is 36.3 °C.

Another product of the ECM process is the formation of hydrogen at the cathode surface. Figure 9 shows in a false color view the volume concentration of electrolyte ϕ_{El}. The corresponding hydrogen volume concentration is $\phi_{H_2} = 1 - \phi_{El}$.
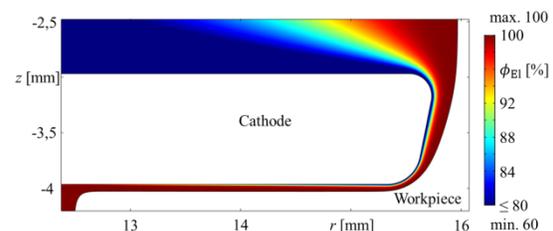
Figure 9. Detailed view of the volume concentration of electrolyte within the working gap at $t = 250$ s

At the beginning of the working gap there is a volume concentration of 100% electrolyte. However, along the cathode surface more and more hydrogen is formed and accumulated in the working gap. At the exit of the working gap, close to the cathode up to 40% of the fluid volume is hydrogen.

Both the temperature and the formation of hydrogen have an influence on the electrical conductivity of the electrolyte in the working gap. This can be seen when regarding the field of the effective electrical conductivity shown in figure 10.
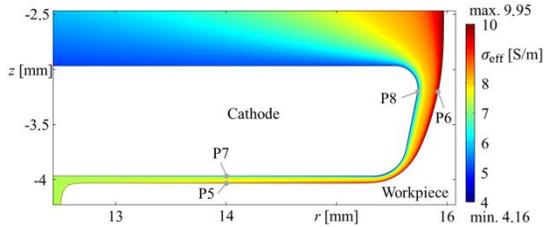
Figure 10. Detailed view of the electrical conductivity field within the working gap at $t = 250$ s

The formation of hydrogen leads to a progressively decreased effective electrical conductivity of electrolyte near the cathode surface. At point P7 the effective electrical conductivity is 5.9 S/m, which is much higher than at point P8 with a value of 4.99 S/m. In contrast to this Joule heating dominates near the anode surface and leads to an increased effective electrical conductivity. At P5 there is a value of 8.93 S/m. In the area of the lateral working gap at P6 the electrical conductivity reaches a maximum of 9.95 S/m.

The totality of the regarded phenomena finally has an influence on the current density distribution within the electrolyte as well as on the current density distribution at the anode surface and in consequence of this also on the material removal. Figure 11 shows the simulated field of the current density magnitude in a detailed view of the working gap at $t = 250$ s.
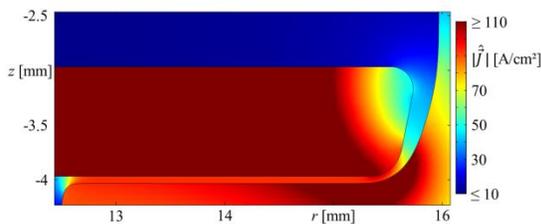
Figure 11. Detailed view of the electrical current density field within the working gap at $t = 250$ s

The current density in the area around the bore is about 10 A/cm². At the entrance of the working gap it rises up to 100 A/cm². This value remains nearly constant over the whole front gap. In the lateral working gap the current density decreases to about 20 A/cm² at the working gap exit.

Based on the current density distribution within the electrolyte the normal electrical current density along the workpiece surface is regarded. Therefore the workpiece surface is divided into 4 sections shown in figure 12 at a machining time of $t = 250$ s.
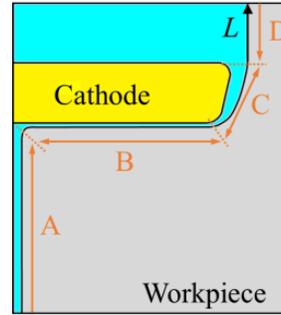
Figure 12. Defined sections along the workpiece surface and the arc length L at $t = 250$ s

Section A corresponds to the surface of the pre-drilled bore. The surface in the front gap area is marked with B. The lateral working gap is section C and D corresponds to the machined surface. Additionally the arc length L is defined on the workpiece surface, which increases along the several sections.

Figure 13 presents the corresponding normal electrical current density along the workpiece surface as a function of the arc length L at $t = 250$ s. The normal component of the current density determines the material dissolution velocity. Here the defined sections of figure 12 are also marked.
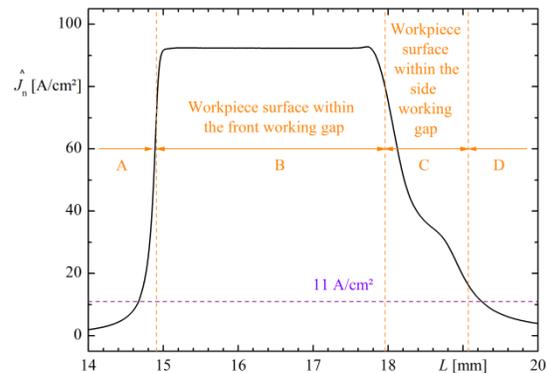
Figure 13. Resulting current density along the workpiece surface as a function of the arc length L shown in figure 12 at $t = 250$ s

Within the bore, there is a current density of approximately 0 A/cm². Here no material dissolution takes place. With decreasing distance to the edge of the bore the current density increases. Due to the transpassive material dissolution behavior of the regarded SAM 10, there is a characteristic current density at which dissolution starts. In this case it is 11 A/cm². At $L = 14.7$ mm the current density exceeds this value. Afterwards the current density rises strongly to a maximum value of 92.5 A/cm. This value remains nearly constant over the whole front working gap in section B. Here the main material dissolution happens. In

section C the current density decreases and for this reason the material dissolution is slowed until it stops in section D. At L = 19.2 mm the current density decreases into the passive range below 11 A/cm² where no further material dissolution takes place.

The final result of the simulation is a deformed geometry of the workpiece. With the presented parameters and cathode a geometry with an internal radius of 16.035 mm and a lateral working gap of 236 µm results.

4. Summary

In this study multiphysics simulations of the electrochemical machining of internal precision geometries were performed. Therefore a 2-D axisymmetric and fully coupled model considering the interfaces fluid dynamics, thermodynamics, electrodynamics as well as geometry deformation was developed. Additionally, the formation and transport of hydrogen was considered in the model. As a first result of the simulation the electrolyte flow, which was modeled as a potential flow, was shown. Here an estimation of the fluid velocities can be made. Further results are the temperature distribution as well as the distribution of hydrogen, which is strongly influenced by the fluid flow. Within the electrolyte a higher temperature causes an increase of the electrical conductivity while a big amount of hydrogen leads to a decreased effective electrical conductivity. For this the influence of the temperature and the distribution of hydrogen on the effective electrical conductivity of the electrolyte was investigated. It arises that locally there is a big range of effective electrical conductivity. For example in the lateral working gap it ranges from 4.99 S/m to 9.95 S/m. This distribution is influencing the current density and in turn the transient material dissolution. Using a material-specific removal velocity function the resulting geometry can be calculated and investigated. Here a geometry with an internal radius of 16.035 mm and a lateral working gap of 236 µm results. On basis of that the simulation model can be used to develop manufacturing processes and to determine important process parameters. This can reduce the amount of required costly and time-consuming experiments.

Acknowledgements

References

[1] A.E. De Barr; D.A. Oliver: Electrochemical Machining. Macdonald & Co. Ltd.,1968. - 248 S.

[2] B. Lauwers; F. Klocke; A. Klink; E. Tekkaya; R. Neugebauer; D. McIntosh: Hybrid processes in manufacturing. In: CIRP Annals - Manufacturing Technology 63 (2014), Nr. 2, S. 561 - 583. – ISSN: 17260604

[3] R. Förster, A. Schoth, W. Menz: Micro-ECM for production of microsystems with a high aspect ratio, In: Microsystem Technologies 11 (2005). S. 246 - 249 Springer-Verlag, DOI 10.1007/s00542-004-0374-7

[4] A. Schubert, G. Meichsner, M. Hackert-Oschätzchen, M. Zinecker, and J. Edelmann. Pulsed Electrochemical Machining of Powder Metallurgy Steels. Proceedings of International Symposium on Electrochemical Machining Technology - INSECT, pages 68-75, 2011.

[5] J. Kozak; K. P. Rajurkar; B. Wei: Modelling and Analysis of Pulse Electrochemical Machining (PECM). In: Journal of Engineering for Industry - Transactions of the ASME 116 (1994), Nr. 3, S. 316-323. – ISSN 0022-0817

[6] J. A. McGeough: Principles of electrochemical machining. London: Chapman and Hall, 1974. – 255 S.

[7] N.N.: Werkstoffdatenblatt 1.4301 der Firma Stahl Markt Engelmann GmbH. Checked on 12.01.2016. http://www.stahl-markt.de/download/datenblatt4301.pdf

[8] N.N.: Werkstoffdatenblatt POM der Firma Wilhelm Herm. Müller GmbH & Co. KG. Checked on 12.01.2016. http://www.whm.net/content/de/download/res/14531-3.pdf

[9] G. Meichsner; M. Hackert-Oschätzchen; M. Krönert; J. Edelmann; A. Schubert; M. Putz: Fast Determination of the Material Removal Characteristics in Pulsed Electrochemical Machining. In: Procedia CIRP, 7th HPC 2016 - CIRP Conference on High Performance Cutting, Volume 46, 2016, S. 123-126, DOI:10.1016/j.procir.2016.03.175